Proceedings of the
Annual Stability Conference
Structural Stability Research Council
San Antonio, Texas, March 19-22, 2024

A Novel Fiber Element to Simulate Interactive Local and Lateral Torsional Buckling in Steel Moment Frames

Arka Maity[1], Amit Kanvinde[2], Diego I. Heredia Rosa [3], Albano de Castro e Sousa[4], and Dimitrios G. Lignos [5]

Abstract
Structural collapse in steel frames under extreme hazards (earthquake, blast etc.) can often be attributed to loss of load carrying capacity of the individual members. Dominant failure modes in structural steel members include interactions between inelastic lateral torsional buckling, global buckling, and local buckling (referred to as Interactive Buckling). Accurate performance assessment of steel moment frames highly relies on the accuracy of the model-based simulations of such limit states. Commonly used concentrated hinge and fiber-based models fail to address the physics of this response leading to inaccurate performance assessment of structures. A nonlinear displacement-based fiber element [named Torsional Fiber Element (TFE)] to simulate monotonic and cyclic interactive buckling in steel members is proposed and implemented on OpenSees (an open-source finite element software). The element includes St. Venant as well as warping torsion response that are essential for lateral torsional buckling response in a wide-flange I-section, through enriched displacement fields and strain interpolation. Response of local buckling is represented in a quantitative manner using a novel multi-axial constitutive relationship with calibration of an effective softening behavior in the post-buckling response. Mesh dependency issue related to the softening material model is also discussed and addressed through a proposed non-local strain measure. The efficacy of the model is assessed through several continuum finite element simulations and experimental data.

1. Introduction

The performance assessment of structures under extreme loading (e.g.- earthquakes) increasingly rely on the accuracy of the model-based simulations, especially nonlinear time history analyses.

[1] Graduate Research Assistant, Department of Civil and Environmental Engineering, University of California, Davis, CA, 95616, USA, arkmaity@ucdavis.edu.
[2] Professor, Department of Civil and Environmental Engineering, University of California, Davis, CA, 95616, USA, kanvinde@ucdavis.edu, Corresponding author.
[3] Graduate Research Assistant, Civil Engineering Institute, Ecole Polytechnique Fédérale de Lausanne (EPFL), Lausanne, 1015, CH, diego.herediarosa@epfl.ch.
[4] Post-doctoral Scholar, Civil Engineering Institute, Ecole Polytechnique Fédérale de Lausanne (EPFL), Lausanne, 1015, CH, albano.sousa@epfl.ch.
[5] Professor, Civil Engineering Institute, Ecole Polytechnique Fédérale de Lausanne (EPFL), Lausanne, 1015, CH, dimitrios.lignos@epfl.ch.

In this context, sophisticated and robust models are required to simulate such nonlinear behavior of the structure till collapse. In steel frames, structural collapse is usually due to the loss in load carrying capacity of individual members combined with the second-order effects due to gravity. As a result, the individual member models should be capable of simulating such failure modes for an accurate assessment of the structure. One of the common failure modes in steel members is nonlinear interaction of local buckling and Lateral Torsional Buckling (LTB), usually called the Interactive Buckling (IB). One form of buckling may precede and trigger the other one and the coupled buckling facilitates a progressive failure of the structure; Fig. 1(a-d) provide an illustration of IB. Numerous experimental (e.g.- Chansuk et al. 2021) and numerical (e.g.- Elkady and Lignos 2015, 2018) studies were conducted on IB; Maity et al. (2023) provides an overview of these. As a result, IB is a well-understood concept. However, well-established simulation models are either numerically expensive (e.g.- Continuum Finite Elements (CFE)) or too simple to include necessary physics behind IB (e.g.- concentrated hinge or spring models). While conventional fiber elements (e.g.- Kolwankar et al. 2018, 2020) show promise by including P-M interactions and spread of plasticity, it still cannot simulate inelastic torsion in I-sections which is relevant to IB. Specifically, they only include direct stress in fibers while shear-axial stress interactions are important in IB and assume Plane Section Remains Plane (PSRP) theory which does not allow simulation of torsional warping. Against this backdrop, two novel formulations are discussed: (1) The Torsional Fiber Element (TFE) which includes shear stresses in fiber as well as torsional warping in the section enabling it to accurately simulate inelastic torsion and hence LTB and IB, and (2) Plate Local Buckling (PLB) multiaxial constitutive model that complements the TFE model by including the effects of local buckling.

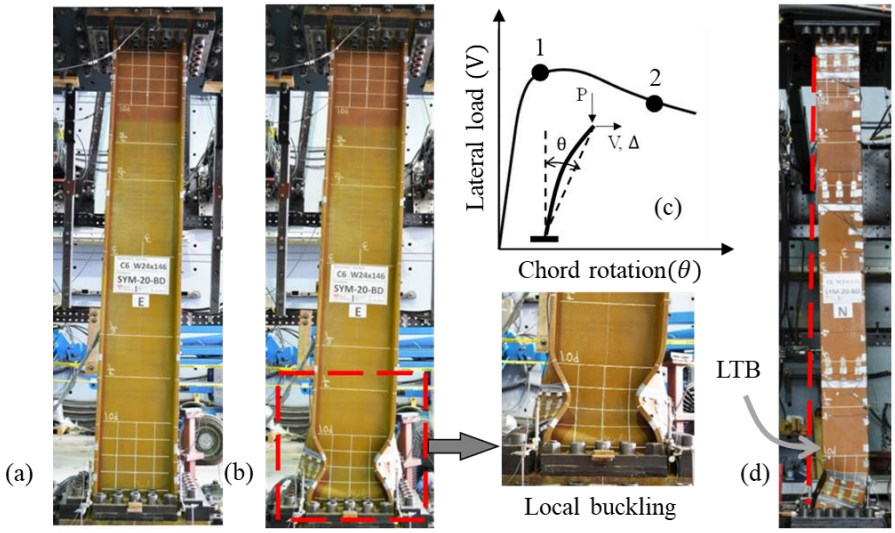

Figure 1: Interactive buckling from representative experiment (Elkady 2016) (W24X146, $P/P_y = 0.2$): major axis views for (a) 2% drift (Instant 1), and (b) 4% drift (Instant 2) and magnified view of local buckling; (c) load-deformation curve marking drift instants 1 and 2; (d) minor axis view showing LTB at 4% drift.

2. Torsional Fiber Element (TFE)

This section presents discussion on the 3d displacement based TFE element construct and numerical implementation. This includes an enriched displacement and strain interpolation in a

wide-flange I-section with the effects of inelastic St. Venant and Warping Torsion along with geometric nonlinear effects.

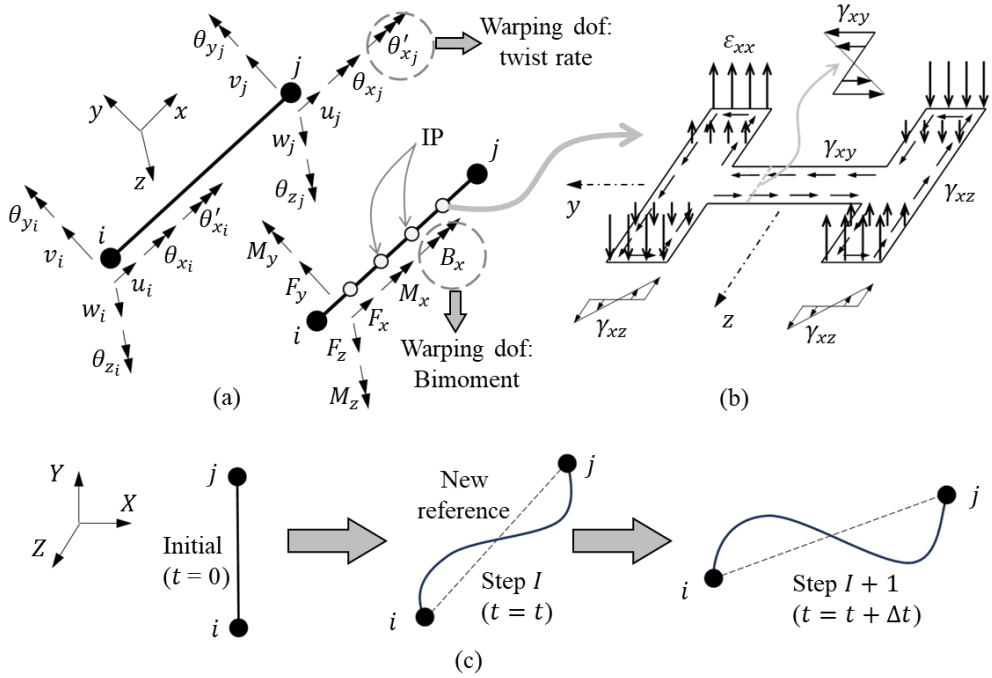

Figure 2: Features of TFE: (a) degrees of freedom including warping, (b) schematic strain distribution in torsion at a typical TFE section, and (c) schematic representation of Updated Lagrangian (UL) geometric nonlinear system.

2.1 Element Construct, Section Kinematics and Strain Interpolation

Fig. 2(a) presents the TFE element and its 14 degrees of freedom (dofs) in contrast with a standard 3d frame element having only 12 dofs. Of these, the two dofs u_i and u_j correspond to axial deformation, while eight dofs ($v_i, w_i, \theta_{z_i}, \theta_{y_i}, v_j, w_j, \theta_{z_j}$ and θ_{y_j}) correspond to flexural and shear deformations; this representation is similar to a standard 3d frame element. However, the torsional deformations are defined using 4 dofs: twist angles (θ_{x_i} and θ_{x_j}) and twist rates (θ'_{x_i} and θ'_{x_j}) at each node. Notably, the twist rate dofs introduces the effects of torsional warping (refer to Maity et al. (2023) for details) in the section and are not present in the conventional Plane Section Remains Plane (PSRP) element; θ'_{x_i} and θ'_{x_j} are considered to be the warping dofs. The work-conjugate for twist rate is the bimoment (B_x) while that of the other displacements are conventional forces and moments (see Fig. 2(a)). This construct is similar to the well-established warping torsion element proposed by Bathe and Wiener (1983). As per the TFE construct, the centerline displacements (u, v, w and θ_x) at any cross-section (at longitudinal location x) can be interpolated as shown in Eq. (1)-(4):

$$u(x) = N_{l_1}(x)u_i + N_{l_2}(x)u_j \tag{1}$$

$$v(x) = N_{c_1}(x)v_i + N_{c_2}(x)\theta_{z_i} + N_{c_3}(x)v_j + N_{c_4}(x)\theta_{z_j} \tag{2}$$

$$w(x) = N_{c_1}(x)w_i - N_{c_2}(x)\theta_{y_i} + N_{c_3}(x)w_j - N_{c_4}(x)\theta_{y_j} \tag{3}$$

$$\theta_x(x) = N_{c_1}(x)\theta_{x_i} + N_{c_2}(x)\theta'_{x_i} + N_{c_3}(x)\theta_{x_j} + N_{c_4}(x)\theta'_{x_j} \tag{4}$$

In the above equations, N_{l_1} and N_{l_2} are standard linear interpolation functions while N_{c_1}, N_{c_2}, N_{c_3} and N_{c_4} represents cubic Hermite interpolation functions (details in Maity et al. (2023)), subscript i and j represent the node numbers. As discussed in the next subsection, these displacement interpolations are applied for incremental displacements as part of the Updated Lagrangian (UL) geometric nonlinearity framework. From the centerline displacements, the continuum displacement field (or fiber displacements) can be found as shown in Eq. (5)-(7):

$$u^c(x,y,z) = u(x) - y\theta_z(x) + z\theta_y(x) - yz\theta_x'(x) \quad (5)$$

$$v^c(x,y,z) = v(x) - z\theta_x(x) \quad (6)$$

$$w^c(x,y,z) = w(x) + y\theta_x(x) \quad (7)$$

The above equations follow a Plane Part Remains Plane (PPRP) assumption (instead of PSRP) where individual flanges and web remain plane after bending; detailed description can be found in Maity et al. (2023). Referring to Eq. (5), the first three terms are the standard PSRP terms found in the conventional 3d frame element while the term $yz\theta_x'(x)$ introduces the torsional warping component and determined only in flanges. This continuum displacement field can be used to interpolate continuum strains. The axial strain component can be obtained by simply differentiating Eq. (5):

$$\varepsilon_{xx}(x,y,z) = u'(x) - y\theta_z'(x) + z\theta_y'(x) - yz\theta_x''(x) \quad (8)$$

In the above equation, the axial strain consists of the deformation variables: axial deformation (u'), curvature (θ_z' and θ_y') and the torsional warping deformation (θ_x''). However, such direct estimate is not available for shear strain in cross-sectional plane (γ_{xy} and γ_{xz}) in an open section. Consequently, a thin-wall idealization was adopted for individual parts (web and flanges) of the section and the shear strains from the St. Venant torsion were obtained (adopting Prandtl stress functions) as:

$$\gamma_{xy}(x,y,z) = -2z\theta_x'(x) \quad (9)$$

$$\gamma_{xz}(x,y,z) = -2y_{flange}\theta_x'(x) \quad (10)$$

where, $y_{flange} = y \mp h/2$ depending on whether the flange is located at $+h/2$ or $-h/2$. Notably, Eq. (9)-(10) creates a shear flow parallel to the longer edge of the any part of the section. The other strain components (ε_{yy}, ε_{zz} and γ_{yz}) are set zero implying there is no distortion in the section, which is supported by the Continuum Finite Element (CFE) outcome. Fig. 2(b)) illustrates the combined strain field in an I-section due to an applied torsion. For details of this strain formulation, refer to Maity et al. (2023). Once the strain field is obtained, a suitable multiaxial material model (discussed in the next section) is used to convert them into stress components (σ_{xx}, τ_{xy} and τ_{xz}) and fed in the global force recovery algorithm (discussed in the next subsection).

2.2 Geometric Nonlinearity and Geometric Implementation

The element construct for TFE is supported by nonlinear geometric effects through an Updated Lagrangian (UL) formulation. This UL formulation includes updating the reference state at the end of every converged step as schematically illustrated in Fig. 2(c). The UL geometric nonlinear system introduces: (1) accurate transformation of load and displacement vectors between local and

global reference by updating the geometry every step, and (2) finite Green-Lagrange strain measure for axial strain (ε_{xx}) which incorporates the axial force-bending-torsion interactions in the formulation (refer to Maity et al. (2023)). The TFE element along with the UL nonlinear geometry formulation were implemented within OpenSees 3.3.0 which has a standard iterative global solution algorithm as shown in Fig. 3. This involves an input of trial global displacement vector ($\boldsymbol{u^g}$) obtained using the applied loads ($\boldsymbol{P_{ext}}$) and tangent stiffness ($\boldsymbol{K_T}$) in each iteration, followed by a standard force recovery process. The output includes an element force vector ($\boldsymbol{P_{int}}$) and tangent stiffness ($\boldsymbol{K_T}$) of the element. $\boldsymbol{P_{int}}$ can be obtained from the interpolated strain and stresses using the virtual work statement. Following the updated reference state, the virtual work statement (for converged state) can be written as a volume integral:

$$\delta_t \boldsymbol{u}.\boldsymbol{P_{ext}} = \int_{V_t} \boldsymbol{T}_t^{t+\Delta t} : \delta_t^{t+\Delta t} \boldsymbol{\varepsilon}(x,y,z)\, dV_t \tag{11}$$

where $\boldsymbol{T}_t^{t+\Delta t}$ is the 2nd Piola-Kirchhoff stress tensor and $\delta_t^{t+\Delta t}\boldsymbol{\varepsilon}$ is the virtual strain tensor for the time increment from t to $t+\Delta t$ (corresponding to step I and I+1, respectively); everything being calculated considering the converged shape at time t as the reference configuration (UL). Through substitutions and simplifications, the internal force can be recovered as:

$$\boldsymbol{P_{int}} = \int_v \boldsymbol{B}^T \boldsymbol{\sigma}\, dv \tag{12}$$

where, $\boldsymbol{B}$ is the derived virtual strain interpolation matrix such that $\delta\boldsymbol{\varepsilon} = \boldsymbol{B}\delta\boldsymbol{u}$. Note that this force recovery was performed based on the incremental input displacements following the UL geometric nonlinearity. Detailed derivation for the force recovery process can be obtained from Maity et al. (2023). Once the internal force is found, the residual $\boldsymbol{R} = (\boldsymbol{P_{ext}} - \boldsymbol{P_{int}})$ is minimized over multiple iterations until found negligible when the system has converged. The other output parameter tangent stiffness ($\boldsymbol{K_T}$) was also obtained in a similar manner as force-recovery such that the j-th column of $\boldsymbol{K_T}$ can be expressed as:

$$\boldsymbol{F^j} = \int_v \boldsymbol{B}^T \bar{\boldsymbol{\sigma}}\, dv = \int_v \boldsymbol{B}^T \boldsymbol{k_m} \bar{\boldsymbol{\varepsilon}}\, dv \tag{13}$$

where, $\boldsymbol{k_m}$ is the material stiffness matrix and $\boldsymbol{F^j}$ is the incremental force vector for infinitesimal incremental strain ($\bar{\boldsymbol{\varepsilon}}$) for infinitesimal incremental displacement ($\bar{\boldsymbol{u}}^{\boldsymbol{j}}$) such that:

$$\bar{\boldsymbol{u}}_i^{\boldsymbol{j}} = \begin{cases} 1, & i = j \\ 0, & \text{i} \neq \text{j} \end{cases} \tag{14}$$

One important aspect of the TFE formulation is that it requires a multiaxial material model to convert strain to stress (see Fig. 3) and return a material stiffness matrix ($\boldsymbol{k_m}$) in the solution algorithm. While this introduces the potential to have a highly interactive nonlinear effects of shear and axial stresses, its efficiency remains highly dependent on a suitable material model. Specifically, a multiaxial model with softening response due to local buckling is necessary to include effects of local buckling while simulating IB. The next section talks about a recently developed material model for local buckling which was adopted for this study.

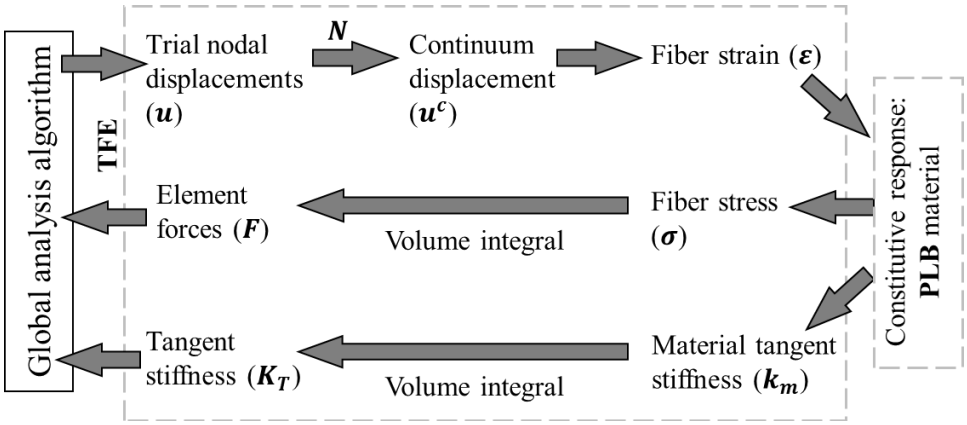

Figure 3: Schematic flow diagram of force recovery with TFE and PLB

3. Plate Local Buckling (PLB) Material

As shown in Fig. 3, the PLB material model was adopted to supplement the TFE in the global analysis scheme. The PLB model developed by the authors (Heredia Rosa et al. 2024) provides a phenomenological representation of an effective softening response due to local buckling through a multiaxial constitutive model. The term 'effective' indicates that the softening is observed only at the member cross-sectional level, not at the continuum level. The popular J_2-plasticity model could not address distinct behaviors in tension and compression due to local buckling as the material should soften only in compression. PLB model addresses this issue by introducing an asymmetric yield surface in tension and compression for local buckling (see Fig. 4(a-c)). Fig. 4(a) illustrates a cylindrical yield surface as observed in J_2-plasticity when the material hardens (see Fig. 4(b)) before local buckling. However, as a result of local buckling, the yield surface on the compression side shrinks into an ellipsoid due to softening (see Fig. 4(c)) while the tension side continues to harden. The yield surface is defined by the following yield function (ϕ):

$$\phi = \begin{cases} \phi^{VM}: 3J_2 - \sigma_y^2 \leq 0 & \text{for } \sigma_H \geq 0;\ \sigma_H \leq 0 \text{ and } \sigma_{c0} \geq \sigma_y \\ \phi^{LB}: 3J_2 + \chi_{1c} I_1^2 - \sigma_y^2 \leq 0 & \text{for } \sigma_H \leq 0 \text{ and } \sigma_{c0} < \sigma_y \end{cases} \tag{15}$$

where, ϕ^{VM} and ϕ^{LB} denote the two parts of the yield surface corresponding to tensile and compressive loading. Note that a positive hydrostatic stress ($\sigma_H = \frac{1}{3} I_1 \geq 0$) represents tension while a negative one represents compression. The terms I_1 and J_2 are the first invariant of stress tensor and second invariant of deviatoric stress tensor respectively while σ_y is the current yield stress. The terms related to softening are: (1) χ_{1c} which controls shrinking ellipsoidal yield surface and is dependent on the stress-state, (2) capping stress (σ_{c0}) representing uniaxial stress at the initiation of local buckling. The parameter χ_{1c} is embedded in the material formulation by Heredia Rosa et al. (2024) while σ_{c0} can be calibrated as described in Section 5. Referring to Eq. (15) the PLB constitutive model is derived from the Updated Voce-Chaboche (UVC) material law (Hartloper et al. 2021) which is a generalization of J_2-plasticity model with combined isotropic-kinematic hardening. The yield surface expansion due to isotropic hardening is defined by the evolution of yield stress (σ_y) with equivalent plastic strain (ε_{eq}^p):

$$\sigma_y = \sigma_{y0} + Q_\infty\left(1 - \exp\left(-b\varepsilon_{eq}^p\right)\right) - D_\infty(1 - \exp(-a\varepsilon_{eq}^p)) \tag{16}$$

where σ_{y0} is the initial yield stress and Q_∞, b, D_∞ and a are the isotropic the hardening parameters discussed in detail by Hartloper et al. (2021). A 2-backstress ($\boldsymbol{\alpha}$) kinematic hardening is controlled by the hardening moduli (C_1, C_2) and recall terms (γ_1, γ_2); details are presented by Hartloper et al. (2021). Note that the PLB model shows hardening response (see ϕ^{VM}) identical to the UVC material in tension. However, in compression, the PLB hardens only until local buckling occurs i.e., when $\sigma_H < 0$ and $\sigma_y \leq \sigma_{c0}$. After this point, the yield surface becomes a shrinking ellipsoid (see ϕ^{LB}) due to softening. This softening is introduced in the yield function by χ_{1c} (see Eq. (15)) which is controlled by the section geometry ($\frac{b_f}{2t_f}, \frac{h}{t_w}$), regularizing parameter (α_{reg}) and capping stress (σ_{c0}). The material parameters and their calibration are discussed in detail in the Section 5. The PLB model was implemented on OpenSees 3.3.0 by the authors; details of this numerical implementation along with a return mapping algorithm can be found in Heredia Rosa et al. (2024)As shown in Fig. 3, the PLB model takes fiber strain (ε_{xx}, γ_{xy}, and γ_{xz}) as input while it returns the fiber stress (σ_{xx}, τ_{xy}, and τ_{xz}) and material tangent stiffness ($\boldsymbol{k_m}$) as output which are used for force recovery as described in the previous section. Note that, the PLB model parameters are calibrated based on Continuum Finite Element (CFE) simulation outcomes for IB; the next section provides details about the CFE modeling.

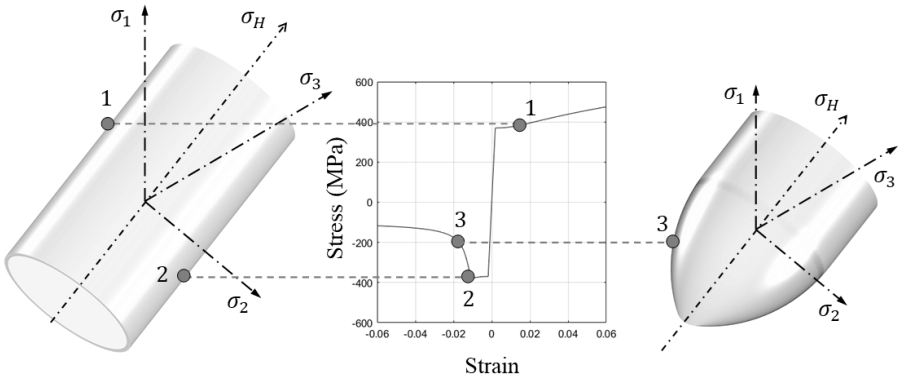

Figure 4: Features of PLB material: (a) cylindrical yield surface in tension and compression before local buckling, (b) corresponding schematic uniaxial stress-strain plot, and (c) yield surface in compression after local buckling.

4. Continuum Finite Element (CFE) Simulations

Benchmark data for verification of TFE model in simulating IB was developed from Continuum Finite Element (CFE) simulations. As a part of this study, the role of CFE simulations include: (1) developing guidelines to calibrate PLB material parameters (discussed in next section), and (2) examination of the efficacy of TFE-PLB combined model in simulating IB response. Table 1 provides a summary of these CFE models. Referring to Table 1, a wide range of parameters were investigated which includes a wide range of cross-sectional ($b/2t_f$, h/t_w) and global slenderness (L/r_y), length (L) and axial load ratio (P/P_y). Two different boundary conditions were also investigated: (1) Fx-Fr: loading end is completely free while other end is fixed, and (2) Fx-Fx: loading end has restrained rotation while the other end is fixed; warping was fixed in both the ends for all the cases. Fig. 5(a-e) provides a representative CFE model (W24X103, Fx-Fx, $L = 5400$ mm, $P/P_y = 0.2$) including deformed shape in IB. The CFE models were developed using the commercial Finite Element Analysis software ABAQUS (2020) following best practices outlined

in Elkady and Lignos (2015). Kolwankar et al. (2018) and Maity et al. (2023) provide a comprehensive overview of the CFE models including material parameter selection and meshing. The key features of CFE models are as follows: (1) Members were discretized into 3d shell elements (S4R on ABAQUS) with element size $\sim 25\text{mm} \times 25\text{mm}$ which is sufficiently small compared to cross-sectional dimensions as well as length of the member. (2) Initial imperfections were introduced both at cross-sectional as well as global level. (3) The Updated Voce-Chaboche (UVC) material constitutive model was adopted with isotropic-kinematic combined hardening; a calibrated set of parameters for ASTM A992 Gr. 50 steel was adopted from Hartloper et al. (2021). Once the IB simulations were conducted, load-deformation as well as spatial distribution of stress-strain were recovered from the CFE models. These results were used to calibrate the PLB material as well as to validate the fully calibrated TFE-PLB combined model. These are discussed in Section 5 and 6 respectively.

Table 1: Simulation set

Specimen	$b_f/2t_f$	h/t_w	L (mm)	P/P_y	Boundary
W24X146	5.92	33.2	5400, 4500	0, 0.2, 0.3	Fx-Fx[1], Fx-Fr[2]
W24X131	6.7	35.6	5400, 4500	0, 0.2, 0.3	Fx-Fx, Fx-Fr
W24X103	4.59	39.2	5400, 4500	0, 0.2, 0.3	Fx-Fx, Fx-Fr
W24X84	5.86	45.9	5400, 4500	0, 0.2, 0.3	Fx-Fx, Fx-Fr
W21X101	7.68	37.5	5400, 4500	0, 0.2, 0.3	Fx-Fx, Fx-Fr

1. Fixed base, loading end with rotational constraints.
2. Fixed base, loading end entirely free.

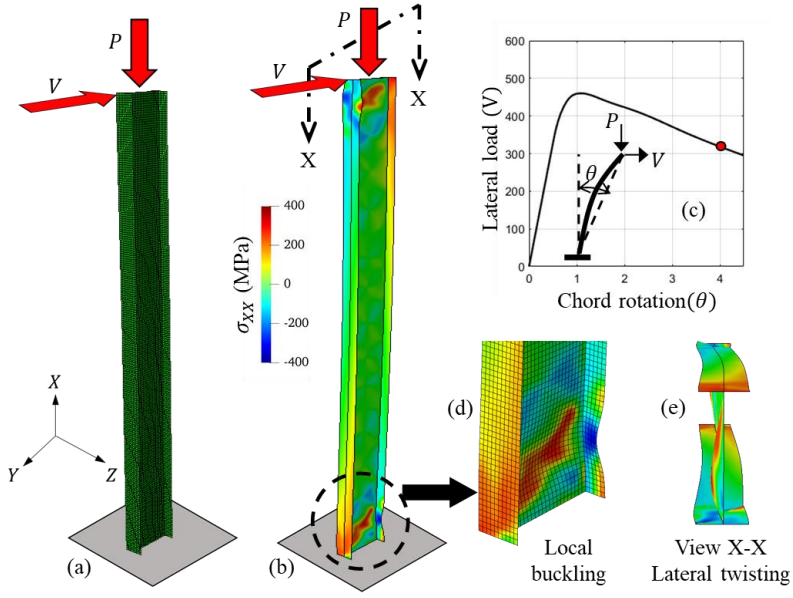

Figure 5: Representative CFE model (W24X103, Fx-Fx, $L = 5400$ mm, $P/P_y = 0.2$): (a) undeformed mesh, (b) interactive buckling at 4% drift, (c) corresponding load-deformation plot, (d) magnified view of local buckling, and (e) sectional view and illustration of twist due to LTB.

5. PLB Material Calibration

The PLB parameters requires calibration before used with TFE to simulate IB response. The entire parameter set can be categorized into three categories and their calibration guidelines are provided in this section.

5.1 Elastic Parameters

These parameters include the fundamental mechanical properties of steel and consist of elastic modulus (E), Poisson's ratio (ν) and initial yield stress (σ_{y0}). These properties can either be directly calibrated from material tests or can be obtained as prescriptive values from established literatures. In this study, parameters for ASTM A992 Gr. 50 steel were adopted from Hartloper et al. (2021).

5.2 Isotropic and Kinematic Hardening Parameters

As discussed earlier, the post-yield response is an isotropic-kinematic combined hardening following UVC material law. Parameters defining such response ($Q_\infty,\ b, D_\infty, a, C_1, C_2, \gamma_1$ and γ_2) usually cannot be directly obtained from standard monotonic tests unlike the elastic parameters. These need to be calibrated from specialized coupon tests with monotonic as well as cyclic loading. Calibrated parameters by Hartloper et al. (2021) were adopted in this study. Note that these hardening parameters are identical to the parameters used in CFE simulations.

5.3 Softening Parameters

The post-local buckling softening response is controlled by two softening parameters (α_{reg} and σ_{c0}) along with the cross-sectional geometry (b_f, t_f, h and t_w); Heredia Rosa et al. (2024) provides a detailed discussion on these parameters. As mentioned earlier, this softening response is 'effective' and does not imply the actual physical response at the continua. As a result, these cannot be obtained from material tests and need to be calibrated based on CFE results. CFE results suggest that softening response for local buckling in web and flanges can be different and require separate calibration. The regularization parameters (α_{reg}^{web} and α_{reg}^{flange}), which control the softening slope based on element size, can be calibrated following guidelines by Heredia Rosa et al. (2024). However, the capping stress (σ_{c0}^{web} and σ_{c0}^{flange}) which marks the initiation of local buckling required a separate calibration for IB. This is because the empirical estimates of σ_{c0} by Heredia Rosa et al. (2024) were based on isolated plate buckling which could not incorporate complex interactions observed in IB. For calibration purpose, a suite of TFE simulations were conducted with trial σ_{c0}^{web} and σ_{c0}^{flange} values and the load-deformation response were compared with CFE results. Following rigorous observation of the results, it was concluded that the capping stress depends primarily on the flange and web slenderness ratio ($\frac{b_f}{2t_f}, \frac{h}{t_w}$) and could be regressed as:

$$\sigma_{c0}^{flange} = 620.31 - 24.191\left(\frac{b_f}{2t_f}\right) - 1.503\left(\frac{h}{t_w}\right) \text{ (in MPa)} \quad (17)$$

$$\sigma_{c0}^{web} = 470.81 - 7.2541\left(\frac{b_f}{2t_f}\right) - 1.1806\left(\frac{h}{t_w}\right) \text{ (in MPa)} \quad (18)$$

The PLB parameters were calibrated for all the test cases in Table 1 and used with TFE for IB simulations. The results and their comparison with CFE are presented in the next section.

6. Result and Discussions

The efficacy of the TFE model largely depends on its ability to simulate inelastic torsion accurately; Maity et al. (2023) provided the validation against experimental result (Farwell Jr and

Galambos 1969). To further verify its effectiveness in simulating LTB strength, two beam bending problems (W24X131 and W24X84, $L = 4500$ mm, simply supported, See Fig. 6(a-e)) were simulated with applied major axis moment (M_Z) at both ends, i.e., $C_b = 1.0$. Both the models were built on OpenSees 3.3.0 with 38 TFE elements (each containing 5 Gauss points) including imperfections (see Fig. 7, discussed later). UVC hardening material was adopted with parameters by Hartloper et al. (2021).

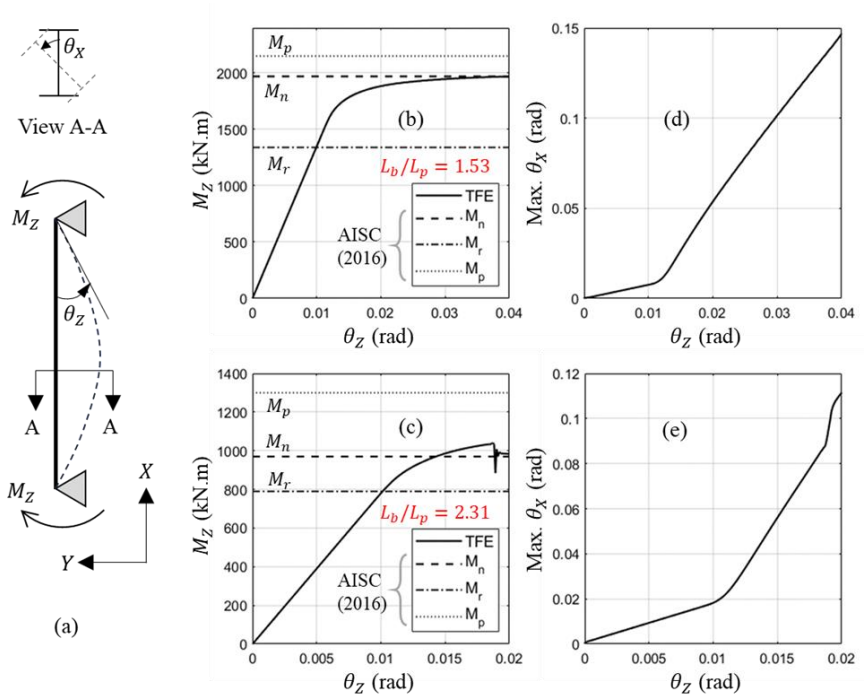

Figure 6: LTB simulations for simply supported beams ($L = 4500$ mm): (a) Applied end moments for $C_b = 1.0$; Moment response (M_Z) for (b) W24X131 and (c) W24X84; Twist response (θ_X) for (d) W24X131 and (e) W24X84.

Fig. 6(a) provides the schematic details of the simulation model while Fig. 6(b-e) provides the outcomes. Referring to Fig. 6(b), the TFE outcome provides a strikingly accurate nominal LTB strength (M_n) prediction (error = ~2%) for W24X131 with $C_b = 1.0$; Fig. 6(d) illustrates an increasing twist response indicating a fully developed LTB. Similar results are presented in Fig. 6(c and e) for the W24X84 beam with $C_b = 1.0$. Referring to Fig. 6(c), TFE slightly overpredicts (~6%) the nominal LTB strength. This was observed because of the relatively slender W24X84 section showing LTB response before yielding in steel. As a result, highly complex buckling modes may appear which the TFE cannot include with the limited degrees of freedom. Considering these, the TFE prediction can be considered a reasonably accurate one.

While Fig. 6(a-e) establish the ability of TFE to predict the LTB strength, to further investigate its ability to predict accurate IB response, the test cases summarized in Table 1 were also simulated using TFE models on OpenSees 3.3.0. Referring to Table 1, a wide range of slenderness ($b/2t_f$, h/t_w, L/r_y), boundary conditions (Fx-Fx and Fx-Fr) and loads (P/P_y) were investigated as they commonly represent members in steel frames. Note that the lengths of the members are relatively

large compared to the plastic LTB length ($L/r_y > L_p/r_y = 42$, for Gr. 50 steel). This implies the members are susceptible to lateral torsional modes which are relevant in IB. Fig. 7(a) schematically represents one representative TFE model. Referring to Fig. 7(a-b), 38 TFE elements were used (typ.), each having 5 Gauss-points. This fine discretization was necessary to accurately simulate the buckled shape and aid the UL nonlinear geometric effects efficiently; details can be found in Maity et al. (2023). Initial imperfections were provided in two forms: (1) initial minor axis displacements (δ_z) to initiate global instabilities (see Fig. 7(c)), and (2) reduced flange thickness (~5%) at potential plastic hinge regions (see Fig. 7(a-b)) to initiate local buckling. Fig. 7(a-b) also schematically illustrate the load and end conditions (Fx-Fr and Fx-Fx respectively).

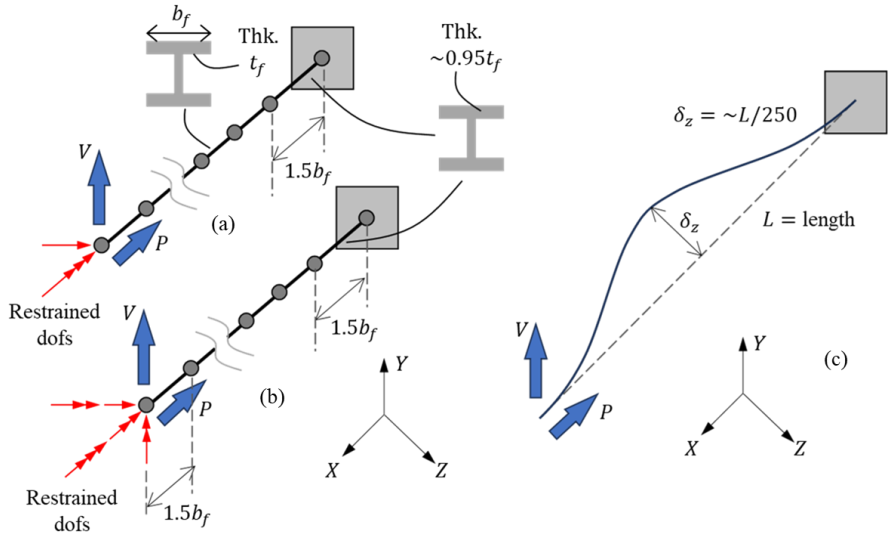

Figure 7: TFE modelling features: schematic meshed model with end conditions and cross-sectional imperfections for (a) Fx-Fr and (b) Fx-Fx end conditions, (c) schematic illustration of global imperfection.

A fully calibrated PLB softening material model for ASTM A992 Gr. 50 steel was used as discussed in the previous section. Notably a softening material model can lead to severe mesh dependency as the strain starts to localize at one element (Wu and Wang 2010) introducing an artificial length scale. An accurate solution relies on either an accurate length scale in elements (e.g.- Maity et al. 2023) or a nonlocal strain formulation at the fibers (e.g.- Kolwankar et al. 2018). In this study a pre-selected the mesh size of $1.5b_f$ were used near potential plastic hinge regions where localization was expected (see Fig. 7(a-b)), following recommendations by Kolwankar et al. (2018). All the models were applied with a displacement controlled transverse load (Δ_Y) following an axial preload (P). Load-displacement as well as spatial distribution of displacement variables were recovered from every simulation. On careful inspection of simulation results, two different buckling response were observed: (1) Buckling is initiated by local buckling while loss in lateral resistance because of plasticity at higher drifts triggers LTB; this was observed in cases with Fx-Fx boundary conditions (see Table 1), and (2) LTB dominates the buckling response as observed in Fx-Fr boundary cases (see Table 1). For brevity, the former is termed as IB dominated response while the latter is called LTB dominated response. Outcomes from one representative example for each type of response are presented as follows.

6.1 Example #1: IB Dominated Response

Fig. 8(a-c) provides the outcome from one representative simulation with TFE model (W24X146, $L = 5400$ mm, $P/P_y = 0.3$, Fx-Fx end condition) showing IB dominated response. Fig. 8(a) presents the load-chord rotation response while Fig. 8(b-c) presents the profile of transverse displacement (Δ_Y) and twist angle (θ_X) along length at 3% drift. Fig. 8(a-c) also overlays the analysis outcome from CFE results. Referring to Fig. 8(a-b), TFE predicted load-deformation response and Δ_Y profile are strikingly similar to the CFE response. However, the θ_X profile suggests a different magnitude of twist occurring in TFE and CFE (see Fig. 8(c)). This can be attributed to the fact that the length scale chosen for this model is specifically for local buckling while the twisted response can localize over a different length. The TFE is still able to capture a qualitatively similar twisted response in IB as observed by CFE. The above-mentioned observations suggest that TFE is capable to simulate IB response in an accurate manner.

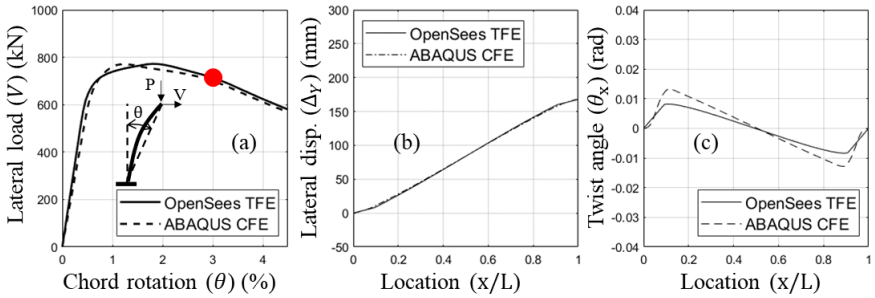

Figure 8: Comparison of TFE vs CFE for (a) load-deformation, (b) lateral displacement profile (Δ_Y) and (c) twist angle profile (θ_X) at 4% drift for representative IB dominated response (W24X146, $L = 5400$ mm, $P/P_y = 0.3$, Fx-Fx end condition).

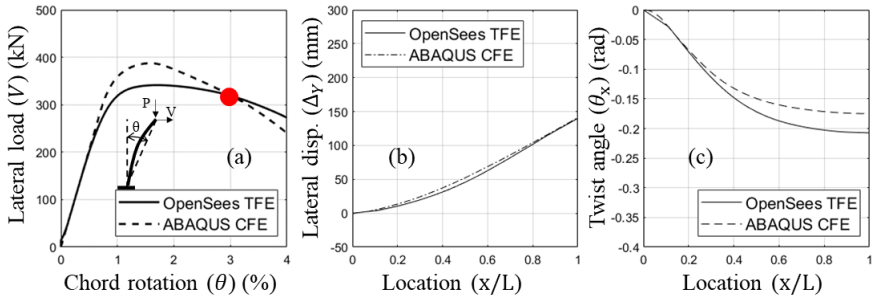

Figure 9: Comparison of TFE vs CFE for (a) load-deformation, (b) lateral displacement profile (Δ_Y) and (c) twist angle profile (θ_X) at 4% drift for representative IB dominated response (W24X131 member, $L = 4500$ mm, $P/P_y = 0.3$ and Fx-Fr end condition).

6.2 Example #2: LTB Dominated Response

Fig. 9(a-c) provides the similar plots for a representative LTB dominated response featuring W24X131 member, $L = 4500$ mm, $P/P_y = 0.3$ and Fx-Fr end condition. Referring to Fig. 9(a) the CFE predicted load-displacement response shows a steeper softening slope compared to the TFE counterpart. This can be attributed to (1) material calibration in TFE-PLB model for local buckling only, (2) limited degrees of freedom in TFE to simulate a complex response with cross-sectional distortions as compared to CFE, and (3) a simplified geometric nonlinearity (UL) as compared to a computationally expensive geometrically exact nonlinear system in CFE. Even with

these limitations, TFE shows a reasonable agreement with CFE simulating LTB dominated response. Fig. 9(b-c) also show close agreements between TFE and CFE for the spatial distribution of transverse displacement (Δ_Y) and twist (θ_X).

7. Summary and Conclusions

Interactive Buckling (IB) is a common failure mode in steel frames especially under earthquakes. Currently available finite element models are either too simple to include necessary physics observed in IB or numerically expensive and impractical for frame analysis. A recently developed displacement-based Torsional Fiber Element (TFE) along with a multiaxial Plate Local Buckling (PLB) material model addresses this issue; both the models were implemented on OpenSees 3.3.0, an open-source finite element software. While the developed model shows potential in capturing accurate response in IB, it still has its own limitations and further scope of research. For example, the model still needs to be verified and upgraded for cyclic loading. Furthermore, the model is still mesh dependent and as per previous studies a nonlocal strain formulation shows promise to eradicate the mesh dependency. These studies are underway by the authors. Once these issues are be addressed, the TFE-PLB combined model can become a robust tool for simulation of steel frames under earthquakes.

Acknowledgements

This work was supported by the US National Science Foundation (Grant number: CMMI-1926202) and by the Suisse National Science Foundation (Award number: 200021_188476), internal fellowships from University of California Davis and an internal research grant from École Polytechnique Fédérale de Lausanne. The findings and opinions presented in this article are entirely those of the authors.

References

AISC. (2016). *Specification for structural steel buildings*. ANSI/AISC 360-16. Chicago, IL: AISC.

Bathe, K.-J., and Wiener, P. M. (1983). "On elastic-plastic analysis of I-beams in bending and torsion." *In Proc., Nonlinear Finite Element Analysis and Adina*. Cambridge, MA: Pergamon. 711–718.

Chansuk, P., Ozkula, G., Uang, C.-M. and Harris III, J. L. (2021). *Seismic behavior and design of deep, slender wide-flange structural steel beam-columns*. Technical Note (NIST TN). Gaithersburg, MD: NIST.

Elkady, A. (2016). "Collapse risk assessment of steel moment resisting frames designed with deep wide-flange columns in seismic regions." Thesis. Montreal: McGill University.

Elkady, A., and Lignos, D. G. (2015). "Analytical investigation of the cyclic behavior and plastic hinge formation in deep wide-flange steel beam-columns." *Bulletin of Earthquake Engineering*, 13 (4): 1097–1118.

Elkady, A., and Lignos, D. G. (2018). "Improved seismic design and nonlinear modeling recommendations for wide-flange steel columns." *Journal of Structural Engineering*, 144 (9): 04018162.

Farwell Jr, C. R., and Galambos, T. V. (1969). "Nonuniform torsion of steel beams in inelastic range." *Journal of the Structural Division*, 95 (12): 2813–2830.

Hartloper, A. R., De Castro E Sousa, A., and Lignos, D. G. (2021). "Constitutive modeling of structural steels: nonlinear isotropic/kinematic hardening material model and its calibration." *Journal of Structural Engineering*, 147 (4): 04021031.

Heredia Rosa, D. I., de Castro e Sousa, A., Lignos, D. G., Maity, A., and Kanvinde, A. (2024). "A fiber-based multiaxial plasticity model with softening for simulating inelastic local buckling in steel beam-columns under monotonic loading" - Under Review. *Journal of Structural Engineering.*

Kolwankar, S., Kanvinde, A., Kenawy, M., Lignos, D. G., and Kunnath, S. K. (2018). "Simulating local buckling-induced softening in steel members using an equivalent nonlocal material model in displacement-based fiber elements." *Journal of Structural Engineering*, 144 (10): 04018192.

Kolwankar, S., Kanvinde, A., Kenawy, M., Lignos, D. G., and Kunnath, S. K. (2020). "Simulating cyclic local buckling–induced softening in steel beam-columns using a nonlocal material model in displacement-based fiber elements." *Journal of Structural Engineering*, 146 (1): 04019174.

Maity, A., Kanvinde, A., Heredia Rosa, D. I., de Castro e Sousa, A., and Lignos, D. G. (2023). “A displacement-based fiber element to simulate interactive lateral torsional and local buckling in steel members.” *Journal of Structural Engineering*, 149 (5): 04023045.

Wu, S., and Wang, X. (2010). “Mesh dependence and nonlocal regularization of one-dimensional strain softening plasticity.” *Journal of Engineering Mechanics*, 136 (11): 1354–1365.